Computational prediction and experimental confirmation of rhombohedral structures in $Bi_{1.5}CdM_{1.5}O_7$ (M = Nb, Ta) pyrochlores†

G. Perenlei,[ab] P. C. Talbot,[ab] W. N. Martens,[a] J. Riches[c] and J. A. Alarco[*ab]

In this study, computationally predicted band gaps and structures using density functional theory (DFT) in $Bi_{1.5}CdM_{1.5}O_7$ (M = Nb, Ta) pyrochlores are confirmed by experimental data on synthesized samples. Ordered Cd substitutions in the B-site of the pyrochlore structures are required to achieve electronic band gaps in the calculated energy band structures, when using full plane waves for DFT calculations, which are supported by a significantly lower total enthalpy. The computationally predicted band gap values are closely matched to experimental band gaps estimated from optical absorption spectra in the UV-Vis. In addition to the prediction of electronic structures, the models also indicate that the large ionic radius of the Cd-cation leads to symmetry modification from the archetypal cubic pyrochlore structure in $Bi_{1.5}CdM_{1.5}O_7$ (M = Nb, Ta). A rhombohedral structure and localized superlattice order are confirmed using X-ray diffraction (XRD) and transmission electron microscopy (TEM) analysis. Energy dispersive X-ray spectroscopy profiles across the superlattice domain interfaces, which are constant within experimental uncertainty, indicate that domain formation is not compositionally driven but likely a mechanism to alleviate strain build up. Raman and FTIR spectroscopy analyses on these two compounds display strong similarities suggesting that peaks and activities belong to the same structure type.

1. Introduction

Pyrochlores, along with perovskites, are ideally cubic structures that allow for significant compositional flexibility, without major changes in crystal symmetries and lattice parameters.[1–4] Their extensive compositional ranges display electronic, ferroelectric, ionic, optical and magnetic properties, which make them useful (and potentially tunable) for a remarkably wide variety of technological applications, including microwave capacitors,[5–7] dielectric materials,[8,9] catalysts,[10–13] gas sensors,[14] solid electrolytes[15] and thermal barrier coatings.[16,17]

Ideal pyrochlores have general formula $A_2B_2O_7$ (sometimes written as $A_2B_2O_6O'$, where O and O' represent oxygen). They can accommodate several combinations of valences of the cation species A and B, including $A_2^{3+}B_2^{4+}O_7$ and $A_2^{2+}B_2^{5+}O_7$, and have been discussed in detail in the literature.[18,19] Oxide pyrochlore structures are composed of two different types of cation coordination polyhedra; the A-site positions are 8-fold coordinated and located within oxygen (O) scalenohedra (at the 16c (0, 0, 0) site in Wyckoff's notation) and the B-site positions are 6-fold coordinated to O and located within trigonal anti-prisms (at the 16d (1/2, 1/2, 1/2) site).[18] The A-site is usually occupied by larger alkali, alkaline earth or rare-earth metal cations, whereas smaller 3d, 4d or 5d-transition metal cations favour the B-site. Oxygen anions are coordinated to metals at both the A sites (with O' on the 48f (x, 1/8, 1/8) sites) and at the B sites (with O on the 8b (3/8, 3/8, 3/8) site).[18]

Many possible cation substitutions at the A and B sites also expand the availability of mixed-valence materials with specific properties of interest.[20] The compositional window and unit cell symmetry of substituted compounds, however, can become more sensitive to the nature of the substituting cations.[20] Structural disorder in pyrochlores is common and it can be promoted by a large ionic size ratio of the A and B cations. The $A_2B_2O_7$ pyrochlore structure remains cubic when the cation size ratio, r_A/r_B, is between 1.46 and 1.78.[18,19] If the ratio exceeds this range, the cubic symmetry is distorted and oxygen vacancies are introduced on the anion sublattice or into the A_2O' network.

Existing families of Bi-based pyrochlores, such as bismuth zinc niobate (α-BZN) and bismuth zinc tantalate (α-BZT) with compositions $Bi_{1.5}ZnNb_{1.5}O_7$ and $Bi_{1.5}ZnTa_{1.5}O_7$, respectively, have been extensively investigated in recent times.[21–25] Both α-BZN and α-BZT have been reported as cubic structures with space group $Fd\bar{3}m$ (No. 227).[26] The crystal structures of BZN and

[a]School of Chemistry, Physics and Mechanical Engineering, Australia. E-mail: jose.alarco@qut.edu.au

[b]Institute for Future Environments, Australia

[c]Earth, Environmental and Biological Sciences Bioscience, Science and Engineering Faculty, Queensland University of Technology, Brisbane, QLD 4000, Australia

BZT consist mainly of Bi and Nb (Ta) cations at the A and B sites, respectively. Zn cations are found to be equally divided between these two sites, with up to 25% of the Bi and Nb (Ta) cations each being randomly substituted by Zn (in a 1 : 3 ratio) according to the Crystal Information Files (CIF) from the Inorganic Crystal Structure Database (ICSD).[26] Thus, the stoichiometric formula of BZN and BZT can be written as $(Bi_{1.5}Zn_{0.5})(Zn_{0.5}Nb_{1.5}O_7)$ and $(Bi_{1.5}Zn_{0.5})(Zn_{0.5}Ta_{1.5}O_7)$, respectively. However, local order of the A-site cations in BZN and subsequent structural relaxation have been determined using neutron and electron diffraction, and Monte Carlo simulations.[27]

Our recent investigations on the electronic band structures of cubic-BZN and cubic-BZT have shown that the use of the (widely accepted) CIFs as inputs for Density Functional Theory (DFT) calculations, result in complete absence of electronic band gaps when using the Full Plane Wave Functions of the Cambridge Serial Total Energy Package (CASTEP) of Materials Studio.[28,29] These results contradict the reported experimental observations of optical band gaps of 3.0–3.2 eV.[30,31] A band gap is obtained for fractional occupancy of cations in BZT using the Linear Muffin Tin Potential.[32] However, the calculated band gap is much lower than experiment and our calculated results for BZT.[29] According to the CIF for BZN and BZT used in these studies, both A and B sites are randomly occupied by Bi/Zn and Nb/Zn (or Ta/Zn) fractional mixtures, respectively.[28,29] In contrast, when the substitutions are considered completely or partially ordered (that is assuming all or part of the substitutions at preferential sites), a remarkable match of calculated electronic band gaps to experimental measurements can be obtained.[28,29]

The DFT calculations on BZN and BZT also predict small modifications from the cubic structure, when complete substitution order is assumed, which appears favoured as attested by the significantly more negative enthalpy of formation.[28,29] However, such favourably calculated modified structures could not be clearly detected by standard X-ray diffraction (XRD) or transmission electron microscopy (TEM) characterizations. An overall cubic structure, predicted by the DFT calculation, could be reconciled by assuming partial order, with order just on the B-sites, while the A-sites remained randomly substituted.[28,29] This final combination also retained a good match between experimentally determined and DFT calculated electronic band gaps.

This current paper investigates the homologous Bi-based pyrochlores using Cd instead of Zn, that is, bismuth cadmium niobate (BCN) and bismuth cadmium tantalate (BCT), and compares the results to those for BZN and BZT. Cd^{2+} has ionic radii of 1.10 Å and 0.95 Å for VIII and VI coordination, respectively, which are significantly larger than the corresponding ionic radii of Zn^{2+} in VIII (0.90 Å) and VI (0.74 Å) coordination, respectively. However, the cation size ratios, r_A/r_B, are 1.60 and 1.65 for both BCN/T and both BZN/T, respectively, when calculated considering the percentage of mixed cations in the both A and B sites ($r_A/r_B = (0.75r_{Bi} + 0.25r_M)/(0.75r_{M'} + 0.25r_M)$) using $(Bi_{1.5}M_{0.5})(M_{0.5}M'_{1.5}O_7)$ M = Zn, Cd; M = Nb, Ta composition). These calculated ratios of BCN and BCT are within the

cubic symmetry ranges as mentioned above. Therefore, this work explores whether Cd substitution in BCN and BCT display more clearly detectable trends with respect to ordering and modification of the cubic pyrochlore structure.

2. Methodology

2.1. Experimental synthesis and characterization

2.1.1. Starting reagents. Powder samples have been prepared by a standard solid-state reaction technique. All starting reagents used in the experiments are of analytical grade (≥99.9%), purchased from Aldrich (Australia). Bismuth oxide (Bi_2O_3), niobium oxide (Nb_2O_5), tantalum oxide (Ta_2O_5), zinc oxide (ZnO) and cadmium nitrate tetrahydrate ($Cd(NO_3)_2$·$4H_2O$) have been used as starting reagents. Stoichiometric amounts of reactants have been weighed to achieve the compositions of $Bi_{1.5}ZnM_{1.5}O_7$ and $Bi_{1.5}CdM_{1.5}O_7$ (M = Nb, Ta). The resultant mixture has been consecutively heated at 400, 600, 800 °C for 1 h and finally at 1000 °C for 5 h followed by intermediate grinding.

2.1.2. Characterization techniques. The structural properties of the synthesized samples have been characterized by XRD. The diffraction patterns have been collected in Bragg–Brentano geometry in the range 10–70° (2θ°) on a spun stage using a Philips PANalytical X'Pert PRO X-ray diffractometer (240 mm radius). The incident X-rays, with Co Kα1 wavelength of 1.78897 Å, have been generated from a PW3373/00 Co X-ray tube, operating at 40 kV and 40 mA. XRD patterns are converted into Cu-radiation using Bragg's equation with Cu Kα1 wavelength of 1.54056 Å. Crystal structure refinements on the XRD diffraction patterns have been carried out using Total Pattern Analysis Solutions (TOPAS, Bruker AXS Version 5) with emission profile and instrumental corrections.

Raman spectra and attenuated total reflectance (ATR) FTIR measurements have been recorded in the range of 100–1000 cm^{-1} using a Renishaw Raman microscope and a Nicolet iS50 ATR-FTIR spectrophotometer, respectively. All measurements have been performed at room temperature, using a He–Ne laser operating at 633 nm with attenuation set to 6. FTIR data have been collected over an accumulation of 4000 scans at a speed of 0.02 min per scan, energy step 0.428 cm^{-1} and resolution of 4 cm^{-1}, to reduce the noise at low frequencies (<200 cm^{-1}).

Optical absorption spectra in the UV-Vis, wavelength regions of 200–800 nm, have been recorded using a UV-Vis-NIR Cary 5000 Stheno spectrometer. The display of the optical absorption spectra have generally been converted from absorbance vs. wavelength to absorbance vs. photon energy.

Additional microstructural characterization has been performed on powder samples dispersed on Lacey formvar/carbon films (300 mesh Cu) using TEM combined with energy-dispersive X-ray spectrometry (EDS). Bright field and high resolution TEM imaging and selected area electron diffraction (SAED) have been obtained using a JEOL JEM-2100 microscope at an accelerating voltage of 200 kV. TEM-EDS analysis has been carried out using an FEI Tecnai TF20 TEM at 200 kV in the scanning transmission electron microscopy (STEM) mode using a low background double-tilt specimen holder. These

techniques have been focused on the identification of potential modifications from cubic symmetry, lattice distortions and defects, and analysis of their crystallography and composition. Image processing of TEM micrographs has been carried out using Gatan's Digital Micrograph software.

2.2. Assumptions for DFT calculations

2.2.1. Input crystal structures. Crystallographic information files (CIFs) for the $Bi_{1.5}CdNb_{1.5}O_7$ (BCN) and $Bi_{1.5}CdTa_{1.5}O_7$ (BCT) compounds are not available in the Inorganic Crystal Structure Database (ICSD) since these compounds have not been characterised in the past. The closest structure reported in the literature is a substitution of Zn^{2+} by Cd^{2+} in the A-site of the $Bi_{1.5}ZnNb_{1.5}O_7$,[33] however, multiphasic material, which differs from our results presented below was obtained. The CIF for BZT (JCPDS card no. 13-6484)[29] has been used as an initial structure for all prepared materials. Therefore, the structure of BCT has been modelled by replacing Cd for Zn in the BZT structure, followed by geometry optimization in the DFT calculation. For the BCN case, the CIF for BZT has been used after replacing both Cd for Zn and Nb for Ta in the structure. The CIF for BZN (JCPDS card no. 16-3002)[28] has also been used to obtain the BCN structure by replacing Cd for Zn. The BCN model from the initial BZT CIF is the preferred alternative as discussed below.

For both BZN and BZT, the CIFs contain 88 atoms in a cubic unit cell and Zn cations are randomly distributed in both the A(Bi) and B(Nb or Ta)-sites. One of the main differences between the CIF for BZN and that for BZT is that the A-site of BZN contains a slightly higher ratio of Bi in the mixed cations when compared to that for BZT. The cubic structures contain fractionally occupied cations in the ratio Bi/Zn = 78.125 : 21.875 and Nb/Zn = 75 : 25 for BZN, and the ratio Bi/Zn = 75 : 25 and Ta/Zn = 75 : 25 for BZT, respectively.[28,29] Another difference between the BZN and BZT structures in the respective CIFs is that the surface of the unit cell of the former contains only metal atoms while the surface of the latter contains only oxygen atoms. Although such a difference after the substitutions, in

principle, is only a translation of equivalent representations of the same periodic structure, our calculations show that the end results are modified in a slightly different manner and adopt different crystal symmetries.[28,29]

For random solid solutions (BCN(r) and BCT(r), where (r) refers to random distribution of Cd in the crystal structure), calculations have been carried out using crystal structures with fractionally occupied (mixed) cations. After substituting Cd for Zn, the resulting fractionally occupied structures have also been further modified by defining specific sites in the crystal structures, where the Cd substitutions take place (BCN(o) and BCT(o), where (o) refers to ordered solid solution). Schematics of the BCN or BCT random and ordered solid solutions using the CIF of BZT as an initial structure before geometry optimization are displayed in Fig. 1. The ratio of Bi to Cd or Nb(Ta) to Cd is [3 : 1] within each unit cell, with substitutions running along the ⟨211⟩ direction as previously described in the literature.[34] Atoms are displayed using a ball and stick style, where Bi, Nb(or Ta), Cd (A and B-sites) and O atoms are purple, blue, green, orange and red balls, respectively, and the diameters of the balls are in proportion to ionic radii. Tables with atomic coordinates of all the atoms within the above mentioned unit cells are given in the ESI in Table S1.†

Structures with ordered substitutions at only a single site (either A or B, while the other site remains fractionally occupied or random) have also been considered as an alternative option for the model structures (BCN(p.o) and BCT(p.o), where (p.o) refers to partial order). Depending on which site the substitution is ordered, the structure is called either A or B-site partially ordered. Details of the structural modifications have been described in our previous publications.[28,29]

2.2.2. Calculated properties, approximations and convergence criteria. Powder diffraction patterns for the BCN and BCT structures with different degrees of substitutional order have been simulated for a Cu X-ray source with a wavelength of 1.54056 Å in Bragg–Brentano geometry using Reflex of Materials Studio (MS) 8.0. Electronic band structure calculations have been carried out using DFT, as implemented in the CASTEP of
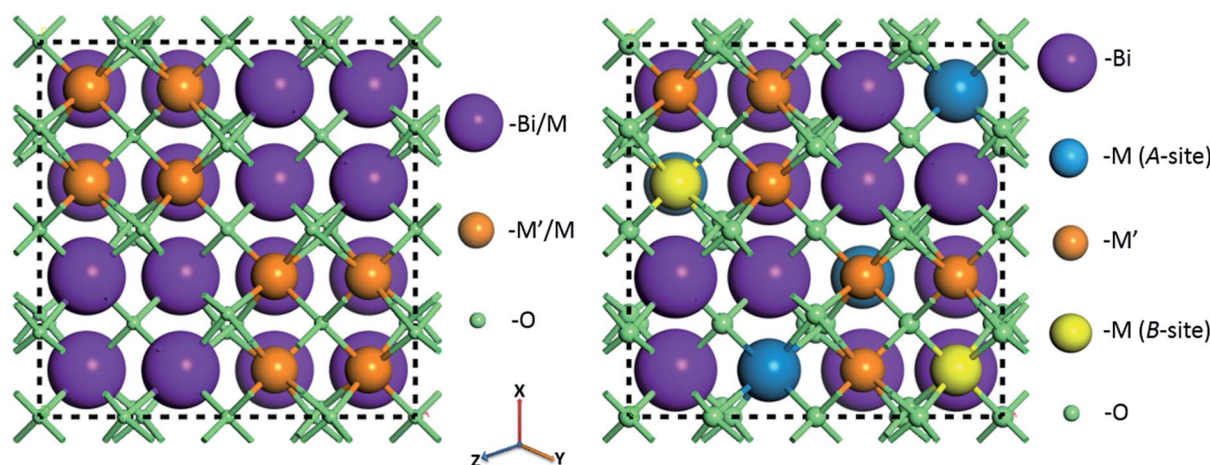

Fig. 1 Crystal structures of $Bi_{1.5}MM'_{1.5}O_7$ (M = Zn, Cd; M' = Ta, Nb) combinations assuming random (left) and ordered (with cations substituted at specific sites) (right) solid solutions before geometry optimization. Full lists with atomic positions are given in ESI (Table S1†).

MS 8.0. All structures have been optimized for geometry and cell parameters. In general, the Generalized Gradient Approximation – with the Perdew, Burke and Ernzerhof (GGA-PBE) exchange correlation functional and norm-conserving pseudopotentials have been adopted in the DFT calculations for random and partially (both A and B-sites) ordered structures, along with k-grid of 0.03 Å^{-1} giving a $6 \times 6 \times 6$ k-point mesh, plane wave basis set cut-off of 830 eV, 100 empty orbitals, non-metal, non-spin, and ultrafine convergence tolerance setups. A customized convergence tolerance has also been used for ordered structural calculations when the standard or default tolerance has resulted in difficulty achieving convergence as mentioned in our previous publications.[28,29] Various pseudopotentials, including norm-conserving, ultrasoft and on the fly, have been applied for DFT calculations on Nb structures due to its strong pseudopotential sensitivity.

3. Results and discussion

3.1. Crystal structure

3.1.1. Experimental XRD patterns. XRD patterns obtained from BCN and BCT powders are shown in Fig. 2. Diffraction patterns for BZN and BZT powders, which have previously been identified as cubic pyrochlore, are also shown in the graph for comparison.[28,29] Peak splitting (shown by the arrows) and broadening can be observed in the diffraction patterns for BCN and BCT, respectively. The observed peak splitting of intense peaks in the BCN pattern, particularly at higher angles, clearly indicates that the structure is not purely cubic. The crystal structure is either modified from cubic symmetry (for example to rhombohedral or orthorhombic) or possibly a mixture of two cubic structures with slightly different lattice parameters. A group that investigated A-site Cd substitution in the BZN structure mentioned a structural distortion from the cubic pyrochlore symmetry.[33] However, due to the multiphasic material, the structural distortion was not well characterized. A local disorder of O′ atoms along the $\langle 110 \rangle$ directions in the crystal structure of BZN has been observed as diffuse scattering in electron diffraction patterns.[27] A sufficiently large distortion in a cubic ($Fd\bar{3}m$) pyrochlore unit-cell can lead to symmetry-lowering and formation of a rhombohedral ($R\bar{3}m$) structure, which will be manifest as peak splitting in the diffraction patterns.[35]

Peak splitting of the most intense peak (for the 222 reflection using cubic indexes) in the diffraction patterns of BCT is not clearly detected at normal scan rates. However, splitting at peaks for (440), (622) and (444) reflections (cubic indices) in the XRD pattern is obtained (see enlarged (440) peak in Fig. 2). The difference between observed BCN and BCT peak patterns may be partly due to a higher sintering temperature ($\geq$1000 °C) required for synthesis of Ta-compounds to a similar level of crystallinity to Nb-compounds.[36,37] In fact, the broader full width at half maximum (FWHM) value can be related to crystallites of smaller size using the Scherrer equation.

Moreover, the diffraction patterns for BZN and BZT, refined to cubic structures with space group $Fd\bar{3}m$ (No. 227) using TOPAS, give lattice parameters $a = 10.558$ and 10.555 Å and fitting coefficients $R_{WP} = 3.86$ and 3.97%, respectively. The
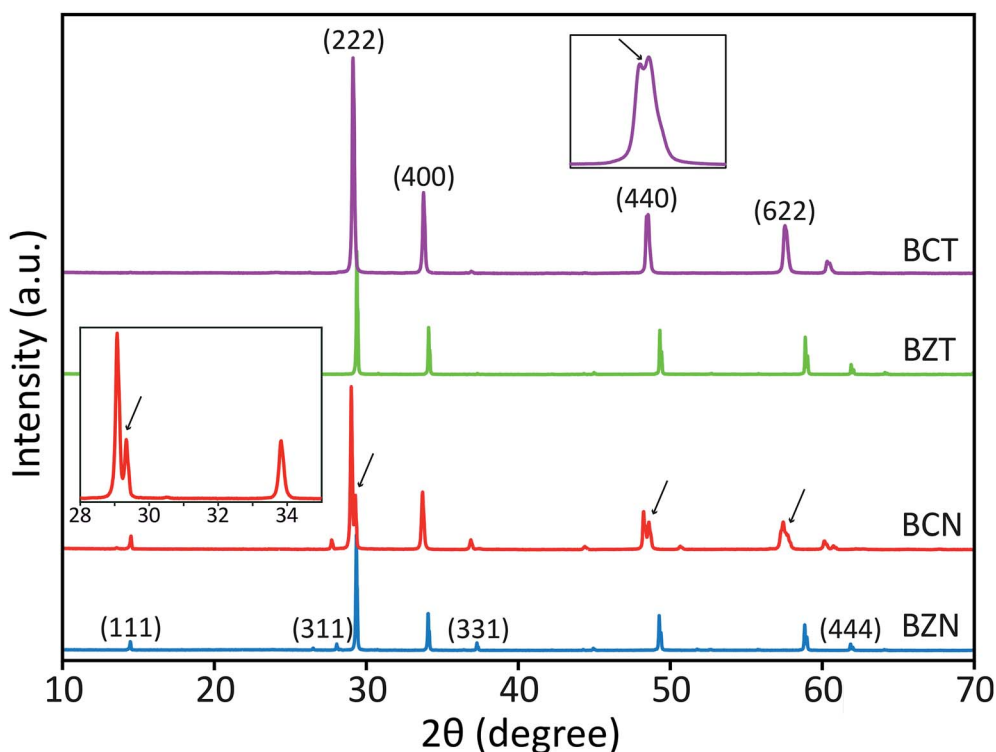

Fig. 2 XRD patterns of BCN and BCT compounds in comparison with those for BZN and BZT compounds, obtained with Cu radiation. The arrows indicate peak splitting and the insets show enlarged portions of the respective coloured patterns.

Table 1 Calculated peak distances and 2 theta angles using (hkl) Miller indices for two coexisting cubic lattices corresponding to the two adjacent (222) peaks in the BCN pattern

h	k	l	TOPAS refined lattice parameter		Calculated from split (222) peak	
			2 theta (°)	Distance	2 theta (°)	Distance
1	0	0	8.303	10.6402	8.360	10.5684
1	1	0	11.753	7.5237	11.833	7.4730
1	1	1	14.407	6.1431	14.505	6.1017
2	0	0	16.650	5.3201	16.764	5.2842
2	1	0	18.632	4.7584	18.760	4.7263
2	2	0	23.631	3.7619	23.794	3.7365
3	1	1	27.786	3.2081	27.978	3.1865
2	**2**	**2**	**29.048**	**3.0716**	**29.249**	**3.0508**
4	**0**	**0**	**33.666**	**2.6600**	**33.901**	**2.6421**
4	4	0	48.350	1.8809	48.700	1.8682
6	2	2	57.399	1.6041	57.825	1.5932

refined unit-cell values for both BZN and BZT are approximated by respective least squares refinements of the (111), (311), (222), (400), (331), (511), (440), (622) and (444) reflections from powder samples as shown in Fig. 2.

When refinements of the BCN and BCT structures to the cubic structure with space group $Fd\bar{3}m$ (No. 227) are attempted, they result in lattice constants $a = 10.640$ and 10.623 Å. The diffraction pattern of BCN fits poorly with $R_{WP} = 22.19\%$, while the pattern of BCT fits more reasonably with $R_{WP} = 8.74\%$. Such poor fitting, particularly for BCN, is due to the large peak splitting at the approximate cubic (222), (440), (622) and (444) reflections in the patterns (see Fig. 2). In this case, the refinement identifies the most intense peak as the (222) reflection for the cubic structure in the diffraction patterns and treats remaining peaks as impurity phases.

Therefore, the possibility of two coexisting cubic structures with slightly different lattice parameters was explored by calculating the expected XRD peak positions for a set of (hkl) Miller indices as shown in Table 1.

Distances are calculated assuming there is a second cubic phase with slightly different lattice parameter. Table 1 shows that if the split peaks around the 2 theta angle (using Cu Kα1 wavelength of 1.54056 Å) around 23.6–23.8° (with (222) indexes) are interpreted as belonging to two cubic lattices with slightly different cubic lattice parameters, other peaks for the same cubic structures (with indexes (400), for instance), should also

display similar splitting according to the table, which is not the case experimentally (see inset on the left for the red XRD trace in Fig. 2). This indicates that two coexisting cubic structures are not an explanation for the peak splitting.

A significantly improved refinement of the BCN pattern, with $R_{WP} = 11.09\%$, has been obtained assuming the structure is better approximated as a rhombohedral symmetry with space group $R\bar{3}crs$ (No. 167). In this case, all peaks, including those split, are indexed and matched with calculated peaks from the TOPAS refinement. The refined rhombohedral lattice parameters of BCN are $a = 10.627$ Å and $\alpha = 90.37°$. Other attempts at refinement with slightly different rhombohedral structures produced fitting parameters as poor as the refinement with a cubic structure. In the case for BCT, both cubic and rhombohedral refinements produce similar quality results, which is due to the absence of obvious peak splitting at the (222) reflection in the diffraction pattern.

Refined lattice parameters for both BCN and BCT assuming both cubic and rhombohedral structures, along with comparative BZN and BZT cubic structures are shown in Table 2. The results for BCT are nearly the same, whether a cubic or a rhombohedral structure is assumed, confirming that the modification of the group symmetry from cubic is minimal (if any). On the other hand, the quality of the fitting for BCN improves in the rhombohedral phase, not only in terms of the overall refinement, but also producing a lattice dimension, which is closer to that of BCT. Both refinements using rhombohedral symmetry are more consistent with the results observed for BZN and BZT compounds.

3.1.2. Simulated powder diffraction patterns. Powder diffraction patterns for the BCN and BCT structures with different assumptions on substitutional ordering simulated in the range between 25 and 65° using Reflex (MS 8.0), are shown in Fig. 3. All diffraction patterns have been simulated from the final geometry optimized structures, including lattice parameters and atomic positions, using DFT calculations. As shown in Fig. 3(a), the main peak positions for ordered and partially ordered structures (the B-site), BCN(o) and BCN(p.o) are nearly the same, while these are shifted to higher angles (that is smaller lattice parameters) for BCN(r). A similar peak shift trend is also observed for BCT(r) when compared with BCT(o) and BCT(p.o) structures as shown in Fig. 3(b). The simulated diffraction patterns of partially ordered structures for both A and B-sites are very similar; thus, results displayed in the graphs are only from the B-site partially ordered structures.

Diffraction patterns for random (BCN(r) and BCT(r)) and partially ordered (BCN(p.o)) structures show single peaks with no peak splitting at the (222), (440) and (622) reflections. However, ordered solid solutions, BCN(o) and BCT(o) (keeping the atomic ratios Bi : Cd = 3 : 1 and Nb (or Ta) : Cd = 3 : 1 in the A and B sites, respectively), have clearly shown double or triple peaks in the simulated diffraction patterns (the arrows indicate peak splitting in Fig. 3). These DFT simulated patterns of BCN(o) and BCT(o) structures in Fig. 3(a) and (b), respectively, closely resemble those obtained from the X-ray diffraction patterns of BCN and BCT samples are shown in Fig. 2. Simulated diffraction patterns of BCT(o) suggest that the peak

Table 2 Refined lattice constants of BCN and BCT compounds compared with those of BZN and BZT

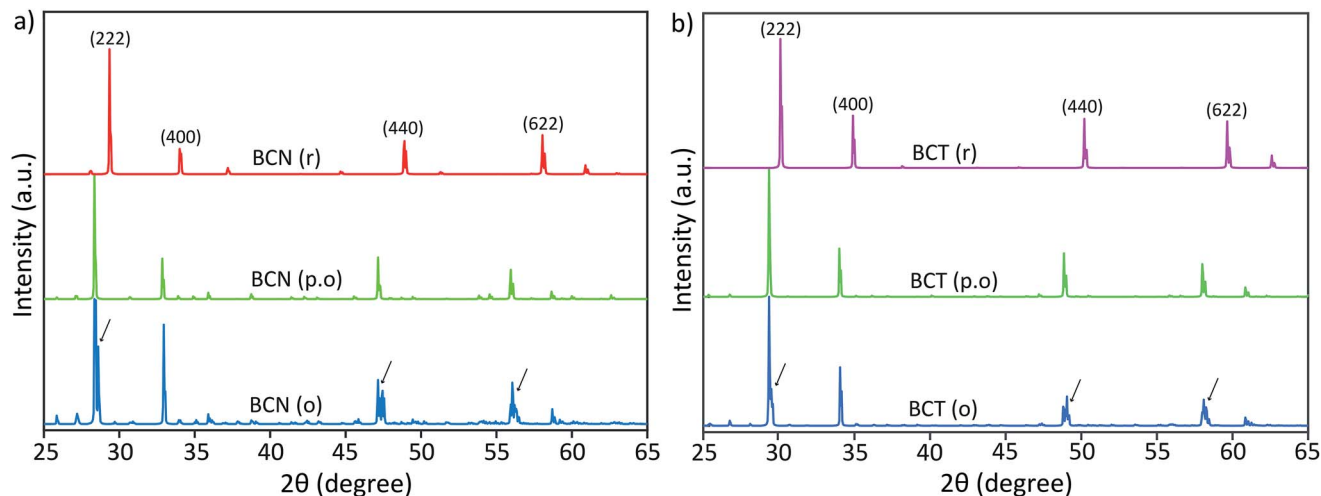| Structure	Cubic		Rhombohedral		
	a (Å)	R_{WP} (%)	a (Å)	α (°)	R_{WP} (%)
BCN	10.640	22.19	10.627	90.37	11.09
BCT	10.623	8.74	10.623	89.98	8.77
BZN	10.558	3.86	—	—	—
BZT	10.555	3.97	—	—	—

Fig. 3 Reflex simulated diffraction patterns of (a) BCN and (b) BCT structures with different cation substitutional order (the arrows indicate peak splitting).

Table 3 Lattice parameters calculated from BCN and BCT with different cation substitutional order, along with those for BZN and BZT structures

| | DFT calculated (geometry optimized) lattice parameters | | | | | Refined lattice parameters from XRD data | |
| | Random | Partially ordered (A-site) | Partially ordered (B-site) | Ordered | | | |
Structure	a (Å)	a (Å)	a (Å)	a (Å)	α (°)	a (Å)	α (°)
BCN	10.532	10.495	10.895	10.867	90.33	10.627	90.37
BCT	10.273	10.173	10.536	10.520	90.25	10.623	89.98
BZN	10.492	10.566	10.822	10.767	90.11	10.558	90.00
BZT	10.223	10.214	10.442	10.418	90.13	10.555	90.00

splitting at major peaks, particularly, at (222) reflections correspond to symmetry modification from the cubic phase and not to a second phase with slightly different cubic lattice parameters.

Small extra diffraction peaks are also observed in the simulated diffraction pattern for the BCN(*o*) structure, which are due to the repeated periodicity of Cd cations in the crystal structure. These small peaks are not observed experimentally, indicating that the superlattice order is not as perfect as simulated, and that it may only exist as few nanometre scale domains. This result suggests that the distribution of Cd cations in the crystal structures is not random, but rather located at specific positions with certain order, at least within a several unit cell domain scale.

Lattice parameters for random, partially and completely ordered BCN and BCT structures after full geometry optimization are shown in Table 2, along with those for BZN and BZT structures. Refined lattice parameters for experimental diffraction data using TOPAS (given in Table 2) are also included in Table 3 for comparison.

3.1.3. Experimental Raman and FTIR. Powder samples have also been examined using Raman and FTIR spectrometry to analyse for structural differences (or similarities) in different compounds, particularly between BCN and BCT and in comparison to BZN and BZT. Fig. 4 shows the Raman spectra for

BZN, BCN, BZT and BCT samples, and for BiNbO₄, which is orthorhombic. The spectra of BCN, BCT, BZN and BZT generally consist of relatively broad peaks or bands, instead of sharper peaks, as shown for BiNbO₄. Broad bands, centred at about 190, 250, 530 and 770 cm^{-1}, which are similar to bands previously reported in the literature,[22] are observed in the BZN Raman spectra. The spectra for BZT is slightly shifted to lower frequencies when compared to the spectra for BZN, yet similar to reports in the literature.[31] The spectra for BCT has slightly sharper peak appearance at low frequencies, but comparable broader band appearance at other higher frequencies. A slight shift and band splitting can be observed in the spectra for the BCN sample when compared to the vibration modes of BZN. In contrast, the entire spectra for BiNbO₄ consists of sharper peaks, which is consistent with reports in the literature.[38]

FTIR spectra (Fig. S1 in ESI†) for all investigated pyrochlore samples and orthorhombic BiNbO₄ have also been collected in the range of 100–1000 cm^{-1} using 4000 sweeps to reduce noise. Consistent with the Raman results, FTIR spectra for the investigated pyrochlores typically has broader peaks than the spectra for the orthorhombic compounds. These results strongly indicate that the investigated pyrochlore compounds have lower symmetry than cubic or orthorhombic, since they would be displaying less degeneracies in their spectra compared to the
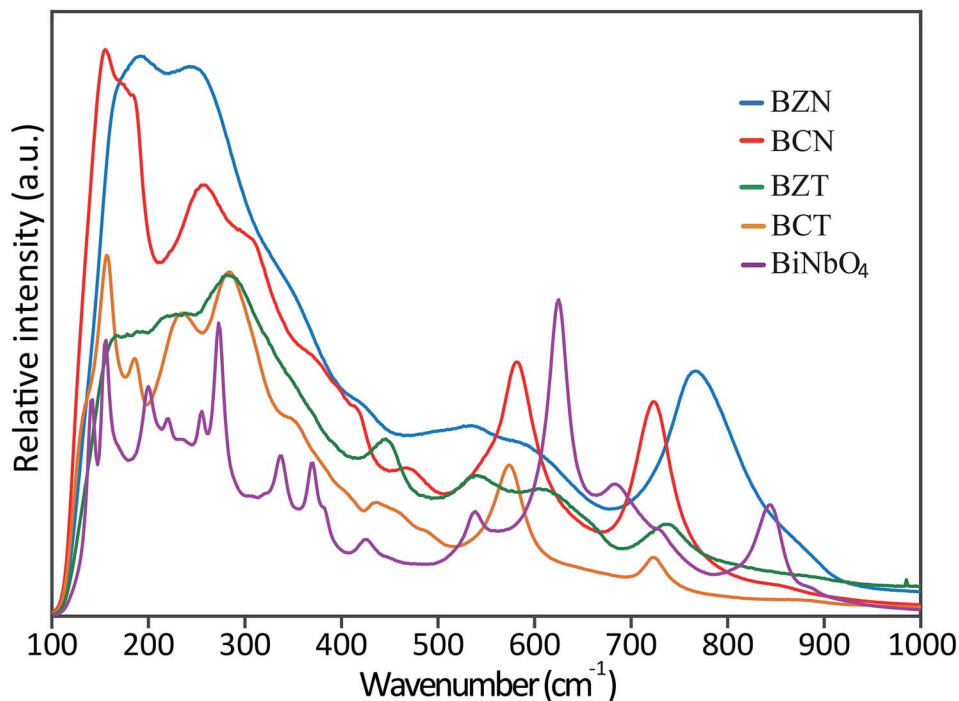
Fig. 4 Raman spectra of BZN, BCN, BCT and BZT samples. The spectra of orthorhombic BiNbO$_4$ is also shown for comparison.

Table 4 Enthalpy comparison for various solid solutions of BCN and BCT structures

	Enthalpy (eV)			
Structure	Random	Partially ordered (A-site)	Partially ordered (B-site)	Ordered
BCN	−55 605.61	−55 812.94	−57 363.54	−57 570.16
BCT	−55 523.88	−55 729.18	−57 381.29	−57 590.19
BZN	−56 059.83	−56 278.83	−58 209.31	−58 427.47
BZT	−55 972.85	−56 188.72	−58 228.60	−58 449.02

more symmetric cubic and orthorhombic structures. Further, the similar appearances and comparable positions between the broad pyrochlore spectra also suggest that these compounds are governed by similar peak position and activity rules, that is, they may belong to the same crystal structure and group symmetry.

3.1.4. Enthalpy. The total enthalpy (or electronic energy) of a particular structure, when compared to other potential phases, is an indicator often used to determine structural stability (*i.e.*, the likelihood that a particular phase will form under the given conditions).[39] This criterion is often applied even when differences are in the meV or sub-meV range. Table 4 shows the obtained enthalpies after geometry optimization of the structures with different substitutional ordering using norm-conserving pseudopotentials.

Differences in calculated enthalpies are substantial and appear to indicate that ordered or partially (B-site) ordered structures are more stable than random or partially (A-site) ordered structures. Specifically, the enthalpy values −57 570.16 and −57 590.19 eV for BCN(*o*) and BCT(*o*), respectively, are considerably lower than the values −55 605.61 and −55 523.88 eV for the BCN(*r*) and BCT(*r*),

respectively. Thus, there are significant differences of 1964.55 and 2066.31 eV for BCN and BCT, respectively, which corresponds to an averaged difference of more than 22 eV per atom (for 88 atoms in the structure).

The situation is similarly stable for the partially ordered solid solutions on the B-site, BCN(p.o) and BCT(p.o), while partial order on the A-site results in enthalpies that are comparable to the random enthalpies. The trends are similar for the BZN and BZT structures as shown in Table 4. Energy minimization is a criterion for geometry optimization and is consistent with the lattice constant comparison discussed in the previous section. Therefore, these results indicate that ordered substitutions of Cd cations in the BCN and BCT at specific sites, followed by slight structural modification from cubic symmetry, minimize the energy.

3.2. Optical properties

3.2.1. Optical absorption measurement. The optical absorption curves in the UV-Vis light region for BCN and BCT powder samples prepared at 1000 °C are displayed in Fig. 5. The
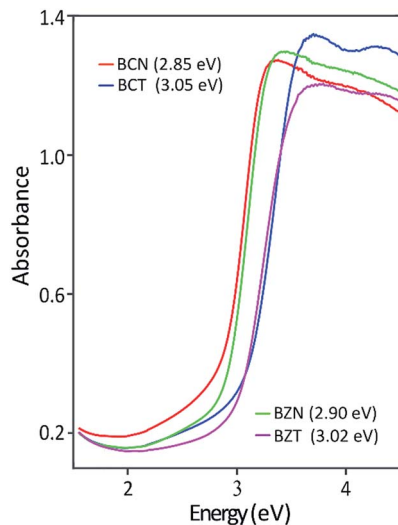
Fig. 5 Optical absorption edges for BCN and BCT powders and comparison with adsorption edges for BZN and BZT.

optical absorption spectra of BZN and BZT samples are also shown for comparison. The experimental band gap values estimated from the onset of absorption edges are about 2.85 eV and 3.05 eV for BCN and BCT, respectively. These values are very close to the corresponding ones for BZN and BZT, respectively.[28,29]

3.2.2. Electronic band structure. Electronic band structures calculated for random solid solution with fractional occupancy of atoms, Bi : Cd = 0.75 : 0.25 and Nb(Ta) : Cd = 0.75 : 0.25 for BCN(r) or BCT(r), have produced metallic-like compounds without electronic band gaps. This situation changes when the substitutions of Cd-cations are assumed to occur at specific, preferential sites in the structures with ratios of Bi : Cd = 3 : 1 and Nb(Ta) : Cd = 3 : 1 for BCN(o) or BCT(o). Clear band gaps evolve between the valence bands (VB) and the conduction bands (CB) at the G-point in the Brillouin zones in the electronic band structures of BCN(o) and BCT(o). Calculated band gaps of about 1.73 and 3.06 eV are obtained for the BCN(o) and BCT(o), respectively, using norm-conserving pseudopotentials.

Furthermore, the electronic band structures produce interesting results depending on the site where partial order has been assumed. Similar to random structures, electronic structure calculations assuming A-site partial order do not display any

band gaps. In contrast, band gaps comparable to those for completely ordered structures are obtained when the Cd-substitutions are partially ordered at the B-site only. However, the partially ordered structures produce a few localized bands in the electronic structures, which are due to the fractional occupancy of the Bi/Cd-cations in the A-site of BCN(p.o) and BCT(p.o).

The calculated band gap values in this case are 1.65 eV (from the dense VB bands to the localized bands) and 2.02 eV (from the dense VB bands to the dense CB) for the B-site BCN(p.o) and 1.74 eV (from the dense VB to the localized bands) and 3.34 eV (from the dense VB to the dense CB) for the B-site BCT(p.o), respectively. Similar behaviour in the electronic structures for BCN and BCT using all the various degrees of order in the structure has been observed for the BZN and BZT structures, as discussed in our previous reports.[28,29]

In the investigated structures, Bi in the A-site is in 8-fold coordination, while Nb and Ta (B-site) are in 6-fold coordination.[40] Bi has p-orbital character, while Nb, Ta and Cd are transition metals and have d-orbital character. This d-orbital character appears to respond to the surrounding crystal field effects to generate a band gap, when periodicities in the substitutions remain under consideration. Random solid solutions destroy the periodicities of the substitutions, and this seems to be reflected in the absence of a band gap. Therefore, ordered solid solution structures appear to be more reliable with regards to the determination of band gaps in electronic band structure calculations using the full plane wave functions of the CASTEP (MS) than randomly substituted solid solutions with fractionally occupied atomic positions. Further, the closing and opening of the gap between the VB and CB is controlled by the B-site (Nb or Ta) cation order.

Table 5 shows the experimentally measured optical band gaps compared with the theoretically calculated band gaps using various pseudopotentials. It can be seen that computed band gap values vary with the pseudopotential options in the DFT calculations. The optically measured band gap value of 3.05 eV is in excellent agreement with the DFT predicted value of 3.06 eV for the BCT(o) using a norm-conserving pseudopotential. In the case for BCN(o), the theoretical band gaps is 1.73 eV using norm-conserving pseudopotential. The computed band gap of 2.55 eV using ultrasoft pseudopotential is closer to the experimental value of 2.85 eV. This result is probably due to a more adequate

Table 5 Comparison of DFT calculated and experimentally observed lattice constants and band gaps

| | Computational data (DFT calculated) | | | | Experimental data | |
| | Norm-conserving pseudopotential | | Ultrasoft pseudopotential | | | |
Structure	Lattice constant (Å)	Band gap (eV)	Lattice constant (Å)	Band gap (eV)	Lattice constant[a] (Å)	Band gap (eV)
BCN	10.867	1.73	10.766	2.55	10.627	2.85
BCT	10.520	3.06	10.989	2.40	10.623	3.05
BZN	10.767	1.76	10.582	2.96	10.558	2.90
BZT	10.418	3.12	10.809	2.71	10.555	3.02

[a] TOPAS refined values.

Nb ultrasoft pseudopotential, which also predicts a lattice parameter more consistent with the experimental result.

3.3. TEM/EDS microstructural characterization

As discussed above, DFT has predicted the largest structural distortion from cubic symmetry will occur in BCN, based on its geometry optimized rhombohedral structure, which has the largest angle. Experimental XRD subsequently has shown that the pattern cannot be matched, let alone refined, to a cubic structure (or to a couple of cubic structures with slightly different lattice parameters). These results identify this material

as a prime candidate for further microstructural characterization to confirm the rhombohedral structure and/or to provide evidence of structural distortion.

Fig. 6(a) and (b) show bright field TEM micrographs, with low magnification, from representative grains of the BCN powder material supported on a holey carbon film. Most grains display an array of parallel domains or bands with alternating contrast when the crystal orientation is suitably aligned with respect to the incident electron beam. A high resolution TEM micrograph from a similar parallel domain region of another BCN crystal is also shown in Fig. 6(a), where it can be seen that
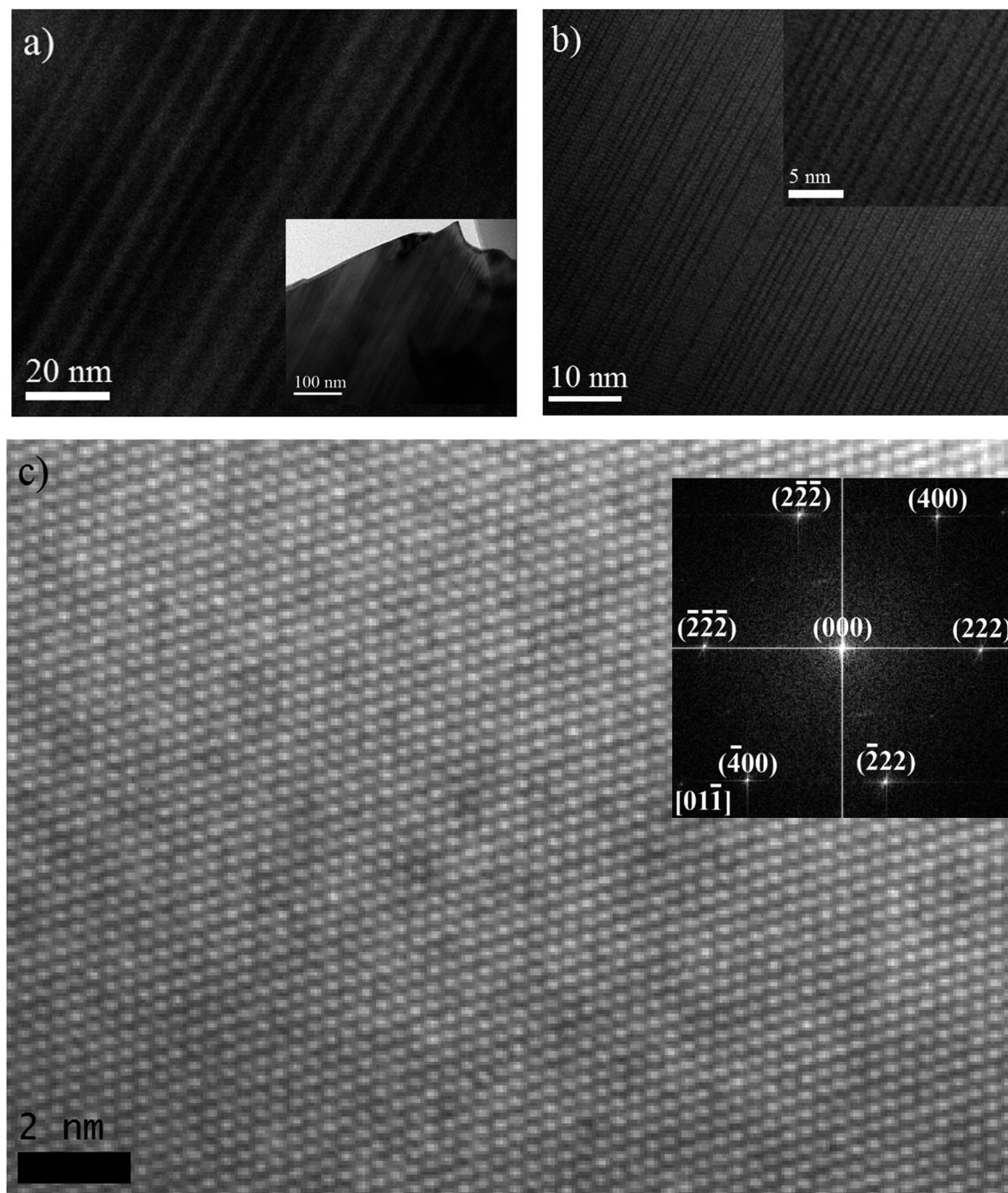

Fig. 6 High and low resolution TEM micrographs and FFT pattern for BCN powders.

many of the boundary planes between adjacent domains correspond to glide planes (highlighted by arrows). The structure of one domain appears to be shifted by half of the lattice spacing along [110] direction on the boundary plane (as described below), relative to the adjacent domain. Formation of this type of stacking fault is generally a mechanism to reduce strain energy in the crystal. Therefore, the TEM observations confirm that the crystal is distorted from cubic symmetry.

Further analysis of the atomic plane distances and angles at adjacent domains can help determine their crystallographic relationships. Fig. 6(c) shows a high resolution TEM image and the corresponding diffraction pattern obtained from the image. The lack of boundaries between domains suggests that this particular crystal is aligned approximately parallel to the interface planes, like those shown in Fig. 6(a, b) and 7(a). Careful measurement of angles in the Fast Fourier Transform (FFT) diffraction pattern indicates that the unit-cell is rhombohedral. In the FFT pattern along the [01$\bar{1}$] direction, the d-spacing of

(222) planes is calculated to be approximately 3.044 Å, which is very close to the d-spacing of 3.047 Å for (222) reflection determined from the TOPAS refinement using a rhombohedral structure.

Fig. 7 shows diffraction pattern obtained from regions indicated by the respective coloured boxes. Dotted lines have been added as guides to more easily visualize similarities between different regions and superposition of electron diffraction patterns occurring in the centre and right regions. The diffraction pattern on the left is indexed to a rhombohedral structure. The diffraction pattern in the centre has in the background, approximately the same pattern as that in the left region, but is superimposed by a finer, more diffuse pattern. This finer pattern has been determined to correspond to a localized superlattice structure (being shorter in reciprocal space, the spots correspond to larger distances in real space). The superlattice spots referred to the rhombohedral lattice show fractional indexes. This confirms new periodicities in
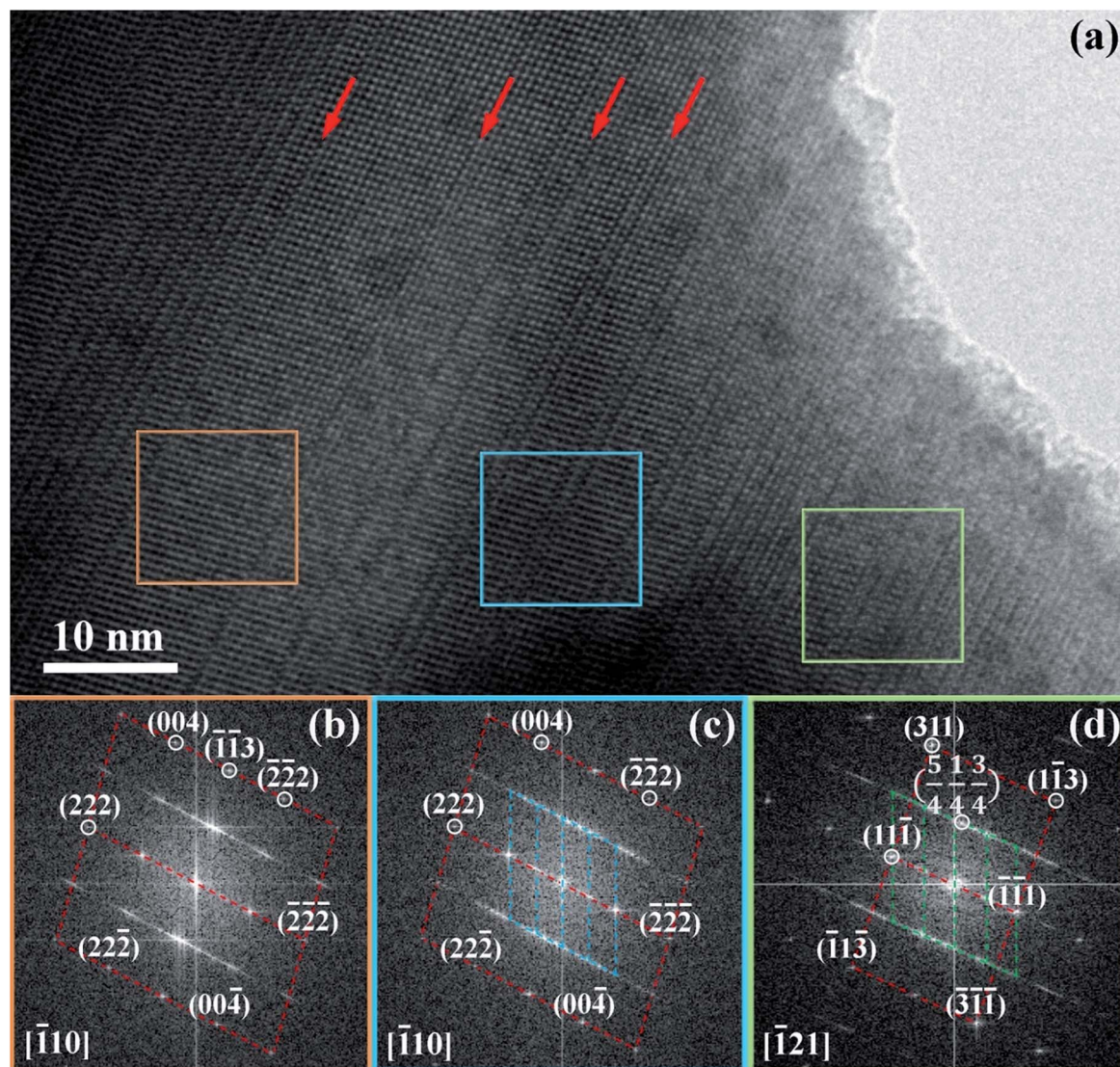

Fig. 7 TEM micrograph and FFT patterns for BCN powders.

addition to the original rhombohedral lattice do exist within these crystals. The diffraction pattern in the right shows a different orientation for the rhombohedral pattern in the background. However, the superlattice spots are approximately the same as those in the centre diffraction pattern. Reciprocal lattices coincident with the background rhombohedral lattice and the superlattice spots can be identified in the centre and right diffraction patterns.

The $[111]$ or $[11\bar{1}]$ directions are perpendicular to the (parallel) interfaces. The $[\bar{1}10]$ and $[\bar{1}21]$ or $[101]$ and $[\bar{1}21]$ directions are along the interface plane. Notice that one of these directions is the observation axis and the other one can be obtained as a vector product between the observation axis and the perpendicular to the interface planes. A superlattice periodicity with indices $\left(\frac{1}{2}, \frac{1}{2}, \frac{1}{2}\right)$ or $\left(\frac{1}{2}, \frac{1}{2}, \frac{\bar{1}}{2}\right)$ also appears to be present, which corresponds to the double lattice period in the high resolution TEM image in Fig. 6(a). It is interesting to notice that the stacking defects at the interface are along $[110]$ directions, which are relevant to the investigations of local order/disorder in the BZN structure.[27] In our previous work, we investigated various choices of substitutional directions. However, the chosen structure in this study is the most representative model.[28] The primary directions, where substitution order is assumed, coincide with the major directions contained in the interface plane.

In order to evaluate whether differences in composition are influencing the formation of domains, EDS line scans (graph is not shown) have been carried out approximately across the perpendicular direction to the domain interface planes. The line scan transects several domains in the sample. On average, the composition remains constant within the uncertainty or noise of the measurement. Small precipitates can be observed to form, even under the more moderate exposure during TEM imaging. They increase in number and coarsen significantly with EDS analysis because this method uses a focussed beam. The spikes in Bi concentration become more pronounced as Bi-rich precipitates appear on the track of the EDS line scan.

The TEM results in conjunction with the XRD analyses consistently and unequivocally show that BCN is rhombohedral as predicted by the DFT calculations. The similar positions and broad appearance of the Raman and FTIR spectra seem to suggest that all the family of investigated pyrochlores may belong to the same crystal structure and group symmetry, that is, they are also very likely rhombohedral. These compounds provide an interesting case for further investigation by XRD using synchrotron radiation. Standard XRD has already displayed indications of peak splitting for BCT, therefore, synchrotron radiation may be expected to fully resolve other peaks in this compound. The situation is not as clear cut for the other pyrochlores, which are closer to the cubic structure, however, it is still worthy of investigation, given the potentially far reaching implications for predictions from DFT calculations. DFT may allow for unprecedented checks and balances to conventional peak fitting, refinement approaches, providing

a more encompassing picture of the combined geometrical and electronic structures.

4. Conclusions

Theoretical DFT predictions for the existence of electronic band gaps in BCN and BCT, which require ordered substitutions in the B-sites and result in structures slightly modified from cubic symmetry, have been experimentally confirmed using a combination of XRD and TEM characterization. Besides excellent agreement between calculated and experimentally determined electronic band gaps, particularly for BCT, formation enthalpies from DFT calculations strongly favour ordered substitutions and the accompanying modifications from cubic symmetry. DFT calculations also indicate that BCN is the most modified case for this substitutional series. It appears that the level of distortion for BCN exceeds a threshold, where the reduced symmetry from an initially assumed cubic structure, becomes clearly manifested in XRD patterns and in TEM as domain formation, presumed to alleviate increasing build-up of strain. The XRD pattern displays splitting of diffraction peaks and high resolution TEM images and electron diffraction patterns from individual domains are consistent with a rhombohedral structure. Remarkably, TOPAS refinement for BCN using a rhombohedral structure is optimal when the initial parameters are close to those predicted by DFT models.

These results are consistent with our previously reported results for BZN[28] and BZT[29] using identical approaches, which indicate that ordered solid solutions are a better approximation to transition metal substitution in this family of Bi-based multi-component pyrochlores when using the full plane wave models in DFT calculations. For the BCN-case, the large size of the Cd cation has apparently magnified distortion effects on the cubic structure, leading to a well-defined rhombohedral structure. The rhombohedral structure has been confirmed by XRD, high resolution TEM and electron diffraction of synthesized samples, and the presence of local superstructures displaying orientation relationships with the rhombohedral axes. These additional periodicities likely correspond to cation order in the material, since detailed compositional analyses at the scale of the superstructures show constant composition across the interfaces.

Comparison of pseudopotentials appears to indicate that norm-conserving pseudopotentials lead to an excellent match between calculated and experimental lattice parameters and band gaps for BCT and BZT. In contrast, results for BCN and BZN significantly improved when ultrasoft pseudopotentials are used, indicating that currently available norm-conserving pseudopotentials for Nb may not be as adequate as their ultrasoft pseudopotentials counterparts. This work constitutes a significant validation of DFT methods for combined determination of geometric and electronic band structures. In addition, this work provides clarity on XRD refinement procedures particularly with regard to appropriate attribution of fractional occupancy of atomic positions in pyrochlore structures.

Acknowledgements

References

1 D. Huiling and Y. Xi, *Ferroelectrics*, 2001, **262**, 83–88.
2 H. Du, X. Yao and H. Wang, *Appl. Phys. Lett.*, 2006, **88**, 212901–212903.
3 X. Fan, R. Sun and X. Wang, *J. Am. Ceram. Soc.*, 2012, **95**(4), 1197–1200.
4 A. Qasrawi, B. H. Kmail and A. Mergen, *Ceram. Int.*, 2012, **38**, 4181–4187.
5 H. Wang, S. Kamba, H. Du, M. Zhang, C. T. Chia, S. Veljko, S. Denisov, F. Kadlec, J. Petzelt and X. Yao, *J. Appl. Phys.*, 2006, **100**, 014105–014107.
6 M. C. Wu, S. Kamba, V. Bovtun and W. F. Su, *J. Am. Ceram. Soc.*, 2006, **26**, 1889–1893.
7 K. Sudheendran and K. Raju, *Ceram. Int.*, 2008, **34**, 897–900.
8 H. Wang and X. Yao, *J. Mater. Res.*, 2001, **16**, 83–87.
9 Q. Wang, H. Wang and X. Yao, *Ceram. Int.*, 2009, **35**, 143–146.
10 Z. Zou, J. Ye and H. Arakawa, *Mater. Sci. Eng., B*, 2001, **79**, 83–85.
11 L. L. Garza-Tovar, L. M. Torres-Martínez, D. B. Rodríguez, R. Gómez and G. Del Ángel, *J. Mol. Catal. A: Chem.*, 2006, **247**, 283–290.
12 Y. Li, G. Chen, H. Zhang and Z. Li, *Mater. Res. Bull.*, 2009, **44**, 741–746.
13 L. Schwertmann, M. Wark and R. Marschall, *RSC Adv.*, 2013, **3**, 18908–18915.
14 Q. Liu, M. Xu, Z.-X. Low, W. Zhang, F. Tao, F. Liu and N. Liu, *RSC Adv.*, 2016, **6**, 21564–21570.
15 A. Qasrawi and A. Mergen, *Ceram. Int.*, 2012, **38**, 581–587.
16 L. X. Pang, D. Zhou and H. Wang, *Ceram. Int.*, 2013, **39**, S673–S676.
17 N. P. Bansal and D. Zhu, *Mater. Sci. Eng., A*, 2007, **459**, 192–195.
18 M. Subramanian, G. Aravamudan and G. S. Rao, *Prog. Solid State Chem.*, 1983, **15**, 55–143.
19 B. C. Chakoumakos, *J. Solid State Chem.*, 1984, **53**, 120–129.
20 L. M. Daniels, H. Y. Playford, J.-M. Grenèche, A. C. Hannon and R. I. Walton, *Inorg. Chem.*, 2014, **53**, 13197–13206.
21 W. Hong, D. Huiling and Y. Xi, *Mater. Sci. Eng., B*, 2003, **99**, 20–24.
22 D. Huiling and Y. Xi, *J. Mater. Sci.: Mater. Electron.*, 2004, **15**, 613–616.
23 H. Wang, R. Elsebrock, T. Schneller, R. Waser and X. Yao, *Solid State Commun.*, 2004, **132**, 481–486.
24 Y. Liu, R. L. Withers, T. Welberry, H. Wang, H. L. Du and X. Yao, *J. Electroceram.*, 2008, **21**, 401–404.
25 C. Khaw, C. Lee, Z. Zainal, G. Miles and A. West, *J. Am. Ceram. Soc.*, 2007, **90**, 2900–2904.
26 X. Wang, H. Wang and X. Yao, *J. Am. Ceram. Soc.*, 1997, **80**, 2745–2748.
27 R. Withers, T. Welberry, A. K. Larsson, Y. Liu, L. Norén, H. Rundlöf and F. Brink, *J. Solid State Chem.*, 2004, **177**, 231–244.
28 G. Perenlei, J. A. Alarco, P. C. Talbot and W. N. Martens, *Int. J. Photoenergy*, 2015, **2015**, 575376.
29 G. Perenlei, J. A. Alarco, P. C. Talbot and W. N. Martens, *Int. J. Photoenergy*, 2015, **2015**, 349030.
30 S. Zanetti, S. Da Silva and G. Thim, *J. Solid State Chem.*, 2004, **177**, 4546–4551.
31 S. M. Zanetti, M. G. S. Pereira and M. C. A. Nono, *J. Eur. Ceram. Soc.*, 2007, **27**, 3647–3650.
32 J. Sun, G. Chen, J. Pei, R. Jin and Y. Li, *Int. J. Hydrogen Energy*, 2012, **37**, 12960–12966.
33 H. Du and X. Yao, *J. Mater. Sci.*, 2007, **42**, 979–982.
34 B. B. Hinojosa, *Atomic structure effects on bulk and surface properties of mixed metal oxides from first principles simulations*, University of Florida, 2010.
35 J. B. Thomson, A. R. Armstrong and P. G. Bruce, *J. Solid State Chem.*, 1999, **148**, 56–62.
36 R. Roth and J. Waring, *Am. Mineral.*, 1963, **48**, 1348.
37 B. Aurivillius, *Arkiv for Kemi*, 1951, **3**, 153–161.
38 H.-F. Zhai, X. Qian, J.-Z. Kong, A.-D. Li, Y.-P. Gong, H. Li and D. Wu, *J. Alloys Compd.*, 2011, **509**, 10230–10233.
39 F. Baletto and R. Ferrando, *Rev. Mod. Phys.*, 2005, **77**, 371.
40 L. Cai, A. L. Arias and J. C. Nino, *J. Mater. Chem.*, 2011, **21**, 3611–3618.